

# **Observing the Sun from start to finish: The Tunable magnetograph's design, calibration, data reduction and scientific exploitation.**

PhD dissertation by

**Pablo Santamarina Guerrero**

Instituto de Astrofísica de Andalucía (IAA-CSIC)

Programa de Doctorado en Física y Matemáticas (FisyMat)  
Universidad de Granada

A thesis submitted in fulfillment  
of the requirements of the degree of  
Doctor of Philosophy

October 25, 2024

PhD thesis supervised by

**Dr. David Orozco Suárez**

**Dr. Julián Blanco Rodríguez**



INSTITUTO DE  
ASTROFÍSICA DE  
ANDALUCÍA



EXCELENCIA  
SEVERO  
OCHOA



**UNIVERSIDAD  
DE GRANADA**



# CONTENTS

<b>1</b>	<b>Introduction</b>	<b>3</b>
1.1	Background . . . . .	3
1.2	Motivation of our work . . . . .	4
1.3	Introduction . . . . .	6
1.4	A brief introduction to spectropolarimeters. . . . .	7
1.4.1	Imaging and optical quality. . . . .	7
1.4.2	Spectroscopy . . . . .	13
1.4.3	Polarimetry . . . . .	13
1.4.4	What do spectrpolarimeters tell us about the Sun? . . . . .	16
<b>2</b>	<b>TuMag’s pipeline and data.</b>	<b>19</b>
2.1	TuMag’s observing modes . . . . .	20
2.1.1	Calibration modes . . . . .	22
2.1.1.1	Flat-field observations . . . . .	22
2.1.1.2	Dark-current observations . . . . .	23
2.1.1.3	Linear polarizer and micropolarizers observations. . . . .	23
2.1.1.4	Pinhole Observations. . . . .	24
2.1.1.5	Straylight target. . . . .	24
2.1.1.6	Prefilter scans. . . . .	24
2.1.1.7	Phase diversity. . . . .	25
2.2	Timelines . . . . .	25
2.3	Pipeline . . . . .	29
2.3.1	Standard data reduccion process. . . . .	29
2.3.2	Extra calibration blocks. . . . .	32
2.3.2.1	Image reconstruction. . . . .	33
2.3.2.2	On-flight polarimetric calibration. . . . .	33
2.3.2.3	On-flight spectral calibration. . . . .	33



rals for page numbers



# CHAPTER 1

---

## INTRODUCTION

### 1.1 Background

In June 2009, the first Sunrise observatory (Barthol et al., 2011) was launched from Kiruna, Sweden, aboard a stratospheric balloon. Equipped with a 1-m aperture telescope, a multi-wavelength UV filter imager, and IMaX, a Fabry-Pérot-based magnetograph, Sunrise was the most complex payload carried by a solar stratospheric balloon to date. Aimed at studying the magnetic fields of the Sun and the dynamics of solar plasma convective flows, the mission was an outstanding success. It resulted in the publication of over a hundred peer-reviewed scientific articles in numerous high-impact journals, including *Astronomy and Astrophysics* (A&A), *The Astrophysical Journal* (APJ), and *Solar Physics*, among others.

Following the success of its inaugural flight, Sunrise embarked on a second journey (Solanki et al., 2017) on June 13, 2013. The primary objective of this subsequent flight was to investigate the active regions of the Sun, as it remained completely *quiet* throughout the entirety of the initial flight. Despite minimal alterations to the instrumentation aboard the observatory, the variance in solar activity during this second flight yielded fresh perspectives and valuable data, ultimately securing the mission success, despite encountering some technical challenges.

Given the success of the first two flights, a third iteration of the Sunrise mission was planned, featuring an updated design. For this third edition, the telescope was equipped with three post-focal instruments: SUSI, a UV spectrograph; SCIP, an infrared spectrograph; and TuMag, the evolution of the IMaX magnetograph. Sunrise III was initially scheduled to fly during the summer of 2020 but was postponed to 2022.

The third launch of Sunrise plays a crucial role in this dissertation. This thesis, initiated in 2020, was centered on the development of the data reduction pipeline for the TuMag instrument, which was entirely developed by the Spanish solar physics consortium. According to the original plan, the first half of the thesis was dedicated to the calibration of the instrument and the preparation of the data pipeline. This way, once the mission was launched, the second half of the thesis could focus on the correction and scientific analysis of the data produced during this third flight. However, this plan (and thus the scope of the thesis) encountered a setback on July 10, 2022, when the third flight of the Sunrise observatory had to be aborted just a few hours after the launch due to a mechanical failure during

the ascent phase.

The observatory was recovered days later after a brief stay in the Scandinavian Alps. Both the telescope and the instruments were found to be in good condition, allowing for the recovery of the observatory and providing hope for a second attempt. However, the process of retrieving the instruments, disassembling, calibrating, and verifying their condition before relaunching the mission is lengthy, and it was not until this year, 2024, that a second attempt became feasible.

In the absence of data produced by Sunrise to process, analyze, and exploit, the scientific work conducted within the framework of this thesis has been compelled to slightly shift its focus. Over these years, we have focused on delving deeper into image correction techniques for data obtained from Fabry-Pérot interferometers, such as TuMag and IMaX. As well as conducting several studies using data products from other instruments, such as the Polarimetric and Helioseismic Imager aboard Solar Orbiter (SO/PHI) and HMI.

It wasn't until the 10<sup>th</sup> of July of 2024 that Sunrise III got its second chance to fly, and this time, the opportunity was not wasted. After a very successful flight that lasted 6 days, the observatory landed in the northern region of Canada on the 16<sup>th</sup> of July. Figure 1.1 shows the trajectory our favourite solar observatory followed over these days. The recovery process started immediately after landing, and we were able to lay hands on the data for the first time on September 2024.

In the following chapters, we will present the work undertaken during the calibration and commissioning of TuMag, conducted in 2021, 2022, and 2024. Additionally, the research carried out between the first and second flights of Sunrise III, which has resulted in the publication of two articles as the main author — one published in APJ and the other in A&A — will also be detailed in this manuscript, as well as other studies that have not yet been published in any scientific journal.

## 1.2 Motivation of our work

In experimental sciences, there is a very strong relation between technological and scientific advances due to the simple fact that we cannot draw conclusions from what we cannot see. We believe it is important for experimental scientists, and more specifically, for observational astronomers, to know the limitations and capabilities and understand the functioning of the instruments we use.

This philosophy is one of the pillars of this thesis, which covers topics ranging from the design and calibration of scientific instruments to the exploitation of the data they produce. With this thesis, we aim to provide a broad, yet detailed, view of the various stages of a scientific mission, from its conception and objectives through its design and calibration, data reduction and preparation for scientific exploitation, and finally, the studies and conclusions derived from it.

In particular, we will detail this process within the framework of solar physics through the development of TuMag, the magnetograph aboard Sunrise III. We will present the scientific objectives of the mission and attempt to link the design concepts with the scientific

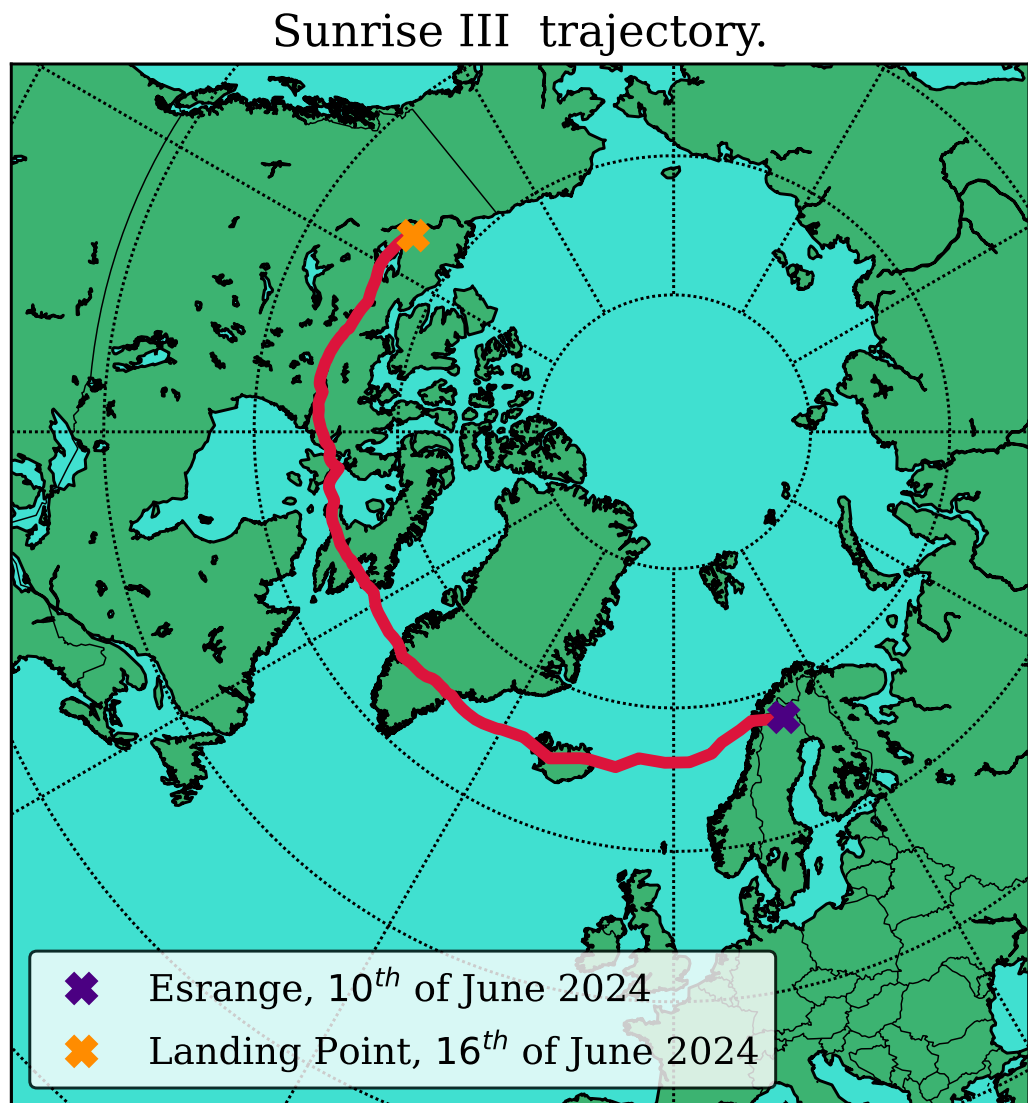


Figure 1.1 Sunrise III trajectory. Aqui poner tambien un foto de sunrise con el globo.

questions we aim to answer. We will address the challenges encountered in data correction due to the technical or instrumental limitations, a subject of ongoing debate within the community and of current relevance. And finally, we also aim to offer a brief dip into the scientific exploitation that can be carried out with the final data product.

With this thesis we aim to clarify the following points:

- ✿ Scientific objectives of TuMag.
- ✿ Instrumental ways of achieving the scientific purposes
- ✿ Open problems for data reduction. Flat-fields, etalon effects in the data.
- ✿ Offering an example of data exploitation with a study case. Persistent Homology.

## 1.3 Introduction

Intro general de la tesis.

Astronomy is one of the broadest fields of knowledge. It studies everything from the smallest astronomical objects, such as the small asteroids that inhabit our solar system, to the global structure and evolution of the universe, including the study of planetary systems, stars, black holes and the galaxies in which they are found. However, despite the diversity of disciplines—ranging from stellar astronomy, radio astronomy, and cosmology, to extragalactic astronomy, astrobiology, and solar physics—they all share a common tool for studying the cosmos: light. Since the very beginning of astronomy, the astronomer's work has been to learn how to modify and measure the properties of the photons that reach us in order to infer the characteristics of the observed object. Although recent advancements have provided astronomers with new lenses to *see* the cosmos, like gravitational waves (**REFERENCIA**) or neutrinos (**REFERENCIA**), among others, light remains as our main resource. Our understanding of the cosmos has always gone hand-in-hand with our ability to design and develop new (or more efficient) and clever ways to dissect the light, spanning from the first solar clocks, passing through Newton's first telescope to the modern-day spaceborne telescopes like the Hubble, James Webb or Solar Orbiter.

Solar physics is no different from other astronomical disciplines in this regard. Our main tool to *see* the Sun is through light. Contrary to what one may think, solar physicists are as photon-starved as any other astronomer. Even though our star is closer and (apparently) brighter than any other astronomical object, our requirements regarding resolution and sensitivity are so high that we are as dependent on extremely optimized instrumentation as any other discipline. Thus, the development of instrumentation employing state-of-the-art technology and techniques plays an important role in modern solar physics.

## 1.4 A brief introduction to spectropolarimeters.

As suggested by the name, spectropolarimeters are instruments designed to measure both the spectral and polarimetric properties of light. In other words, they assess the polarization state of light as a function of wavelength. Their use is widely extended in astrophysics, owing to the substantial amount of information that can be inferred about the light source from these properties.

There are two distinct types of spectropolarimeters, distinguished by their approach to spectroscopy: slit-based spectrographs and narrow-band tunable filtergraphs. The latter preserve spatial resolution by capturing two-dimensional images of the solar scene at the expense of sacrificing spectral resolution. Conversely, slit-based spectrographs provide excellent spectral resolution but have a limited spatial resolution.

Regardless of the method employed for spectroscopy, spectropolarimeters must be able to measure the polarization state of light, in other words, they must determine the Stokes parameters of the incident light. These four parameters, typically expressed as a pseudo-vector,  $[I, Q, U, V]$ , were introduced by Stokes (Stokes, 1851) as a formalism to fully describe the polarization state of light. The first parameter,  $I$ , denotes the total intensity, while  $Q$  and  $U$  provide information on the intensity of linearly polarized light at  $0^\circ$  and  $90^\circ$ , respectively. Lastly,  $V$  represents the intensity of circularly polarized light.

Outstanding polarimetric sensitivity and spectral resolution are rendered ineffective if the optical capabilities of the instrument are not up to par. The design of these instruments must achieve diffraction-limited imaging, coupled with a signal-to-noise ratio that ensures a polarimetric sensitivity for stokes  $Q$ ,  $U$  and  $V$  of approximately 1000. Additionally, it must provide the best spatial resolution that the telescope allows, all while maintaining high spectral resolution and minimizing observation time. Consequently, instrument design requires a careful balance among these three properties: spectral, optical, and polarimetric capabilities.

In the following sections, we will examine each of these aspects in greater detail, with a particular emphasis on filtergraphs. Tunable filtergraphs play a significant role in this thesis, as the primary blocks of scientific work presented herein have been conducted for TuMag, a tunable magnetograph, as well as etalon-based instruments in general. Consequently, our description will be tailored to these types of instruments. It is important to note that much of the information provided will be generic and applicable also to slit-based spectrometry; however, certain specific behaviors will be unique to filtergraphs.

### 1.4.1 Imaging and optical quality.

Filtergraphs are, first and foremost, imagers. The high-resolution imaging that filtergraph instruments are capable of is one of the pivotal reasons for their extended use. The ability to capture a two-dimensional scene of the solar surface makes them ideal for studying solar plasma structures, which require resolutions close to 100 km on the solar photosphere. These instruments must be able to ensure an image quality and resolving power enough to measure these structures. For this reason, we will begin our description of the filtergraphs

with a brief explanation of image formation and image quality assessment.

Let us assume that the extended source we are observing has an intensity distribution in the image plane given by  $O(\xi_0, \eta_0)$ . Then, if we assume a linear optical system and incoherent illumination, the intensity distribution measured at a point  $\xi, \eta$  of the image plane is given by :

$$I_j(\xi, \eta; \lambda_s) = \iint O(\xi_0, \eta_0) S(\xi_0, \eta_0; \xi, \eta; \lambda_s) d\xi_0 d\eta_0, \quad (1.1)$$

where  $S(\xi_0, \eta_0; \xi, \eta; \lambda_s)$  represents the imaging response of the instrument, also referred to as the Point Spread Function (PSF). The PSF describes the normalized intensity distribution in the image plane when observing a point source, which, due to diffraction and inherent imperfections in any imaging system, cannot be imaged as an ideal point.

The PSF is crucial in the assessment of image quality and resolving power of an instrument since it defines how fine detail will be imaged into the detector. One particularly relevant metric for image quality assessment that can be derived from the PSF is the optical transfer function (OTF), which is the Fourier transform of the PSF (Vargas Dominguez, 2009).

$$OTF(\nu) = \hat{S}(\xi_0, \eta_0; \xi, \eta; \lambda_s), \quad (1.2)$$

where the operator  $\hat{\cdot}$  is the Fourier transform, and  $\nu$  represents the frequency vector in the Fourier domain.

The OTF describes how different spatial frequencies are transferred from the object to the image, thus characterizing the system's ability to resolve fine details. However, since imaging systems measure intensities, we are primarily concerned with how the intensity pattern of an object is transferred to the image. A key metric for quantifying this transfer is modulation, or contrast, which is defined as the ratio between the peaks and valleys of intensity at a given spatial frequency:

$$M_\nu = \frac{I_{max}^\nu - I_{min}^\nu}{I_{max}^\nu + I_{min}^\nu}. \quad (1.3)$$

The function that encodes the dependency of the modulation with spatial frequencies is called the modulation transfer function (MTF), and is strictly related to the OTF as the ratio of the modulation of the object  $MTF_{obj}$  and that of the image  $MTF_{im}$  can be computed from the magnitude of the OTF (Gaskill, 1978):

$$MTF = \frac{MTF_{im}(\nu)}{MTF_{obj}(\nu)} = |OTF(\nu)|. \quad (1.4)$$

From this definition, it is evident that a perfect optical system would have an  $MTF = 1$  at all spatial frequencies, meaning that all details are perfectly transferred from the object to the image. However, real optical systems exhibit a decrease in MTF as spatial frequency increases. In practice, the resolution of an optical system can, and is often defined as the spatial frequency at which both the MTF and, consequently, the OTF reach zero (Tyson,

2000). This threshold frequency marks the limit beyond which the system can no longer resolve finer details.

Another key concept for assessing the imaging performance is the phase error or wavefront. The wavefront of an optical system is defined as the deviation in phase at any point within the image from that of an ideal spherical wavefront (Snyder, 1975). Such deviations arise from various optical imperfections within the imaging system, and their impact on image quality depends on the specific nature of the aberration. For instance, imperfections in mirror shape or lens configuration can result in spherical aberrations, leading to a broadening of the PSF and a subsequent reduction in resolution. Other common aberrations include astigmatism, where the focal point varies along different axes, producing distorted images, and comatic aberrations (coma), which can occur due to misalignment of optical elements and manifest as tail-like distortions in the images of point sources.

It is common to see requirements or assessment of the optical quality of optical instruments in terms of the root mean square (rms) of the variance of the wavefront,  $\Delta\phi(\xi, \eta)$ , usually referred to as the wavefront error (rms WFE) or simply WFE:

$$WFE = \sqrt{\frac{1}{A} \int_A (\Delta\phi(\xi, \eta))^2 d\xi d\eta}, \quad (1.5)$$

where  $A$  is the area of the aperture.

This value, essentially the standard deviation of the wavefront across the aperture, is closely tied to beam propagation quality. In fact, it can be demonstrated that the wavefront variance can be derived from the Strehl ratio, or viceversa. The Strehl ratio is defined as the ratio of the peak intensity of a point source in an aberrated system to that of an ideal system operating at the diffraction limit. It is one of the most widely used metrics for assessing the optical quality of a system, ranging from 1, for a perfect, unaberrated system, to 0. For small aberrations, the Strehl ratio (SR) and WFE are related by the following expression (Snyder, 1975):

$$SR \simeq \exp \left[ - \left( \frac{2\pi WFE}{\lambda} \right)^2 \right]. \quad (1.6)$$

Although the Strehl ratio and rms WFE provide a concise measure of the optical quality of a system, the WFE contains additional information regarding imaging performance. Rather than relying solely on a single averaged value (such as the standard deviation), the wavefront can be represented as a two-dimensional map projected onto a plane normal to the light path, typically the image plane. To carry out such a representation analytically, it is essential to select an appropriate mathematical framework. Given the widespread use of circular apertures in telescopes, mirrors, lenses, and other optical components, it is advantageous to approach the problem using polar coordinates,  $\rho$  and  $\theta$ , and in particular, to employ an orthonormal basis for the interpretability of the results. Among the multiple (infinite) sets of polynomials that fulfill these requirements, the Zernike polynomials (Zernike, 1934) offer some distinct advantages. The Zernike polynomials are a sequence of polynomials that compose an orthonormal basis over a unit circle. Given an arbitrary wavefront,

$(W(\rho, \theta))$ , the expansion in terms of the Zernike polynomials can be expressed as:

$$W(\rho, \theta) = \sum_{n,m} C_n^m Z_n^m(\rho, \theta), \quad (1.7)$$

where  $Z_n^m$  are the Zernike polynomials,  $C_n^m$  are the amplitudes of the coefficients in the expansion and  $n$  and  $m$  are the radial order and angular frequency, respectively. The Zernike polynomials can be obtained from:

$$\left. \begin{array}{l} Z_n^m(\rho, \theta) = R_n^m(\rho) \cos(m\theta), \text{ for } m \geq 0, \\ Z_n^{-m}(\rho, \theta) = R_n^m(\rho) \sin(m\theta), \text{ for } m < 0, \end{array} \right\} \quad (1.8)$$

where  $R_n^m(\rho)$  are the radial functions given by:

$$R_n^m(\rho) = \sum_{l=0}^{(n-m)/2} \frac{(-1)^l (n-l)!}{l! [\frac{1}{2}(n+m)-l]! [\frac{1}{2}(n-m)l-]!} \rho^{n-2l}. \quad (1.9)$$

This representation of the wavefront is particularly valuable because each mode, defined by a specific pair of  $n$  and  $m$  values, corresponds to a distinct aberration in the wavefront, with the associated coefficient representing the contribution to the rms WFE for that specific aberration. Furthermore, the orthogonality of the Zernike basis ensures that adding additional terms to the expansion does not influence the values of previously calculated coefficients. In other words, the Zernike polynomial expansion enables the wavefront to be expressed as the sum of individual aberrations, providing a clear decomposition of the wavefront errors.

Figure 1.2 presents an example of a simulated wavefront, including a two-dimensional cross-section and the individual Zernike components of the simulation. The simulation incorporates only the first ten Zernike polynomials, corresponding to polynomials with  $n \leq 3$ , which account for aberrations such as defocus, astigmatism, coma, and trefoil, among others. For a comprehensive overview of the Zernike expansion in wavefront characterization, we direct the reader to Lakshminarayanan & Fleck (2011).

Although properties such as the PSF and WFE provide us with a lot of information to evaluate the instrument's performance, they are not known a priori. Instruments need to be equipped with means to measure these quantities in order to assess the performance and correct for any defects. The strategy to follow depends on the specific characteristics of the instrument. For instance, ground-based instruments can be equipped with adaptive optics systems, where the wavefront is directly measured and corrected in real time (REFERENCES). However, this approach is not feasible for all instruments due to the technical demands required to implement such corrections. In these cases, alternative techniques, such as the phase diversity method, are necessary.

The phase diversity algorithm (Childlaw et al., 1979) is a method to infer the aberrations present in an optical system by obtaining, at least, two simultaneous, or quasi-simultaneous, images of the same object where an additional and known aberration is introduced to one of the images.

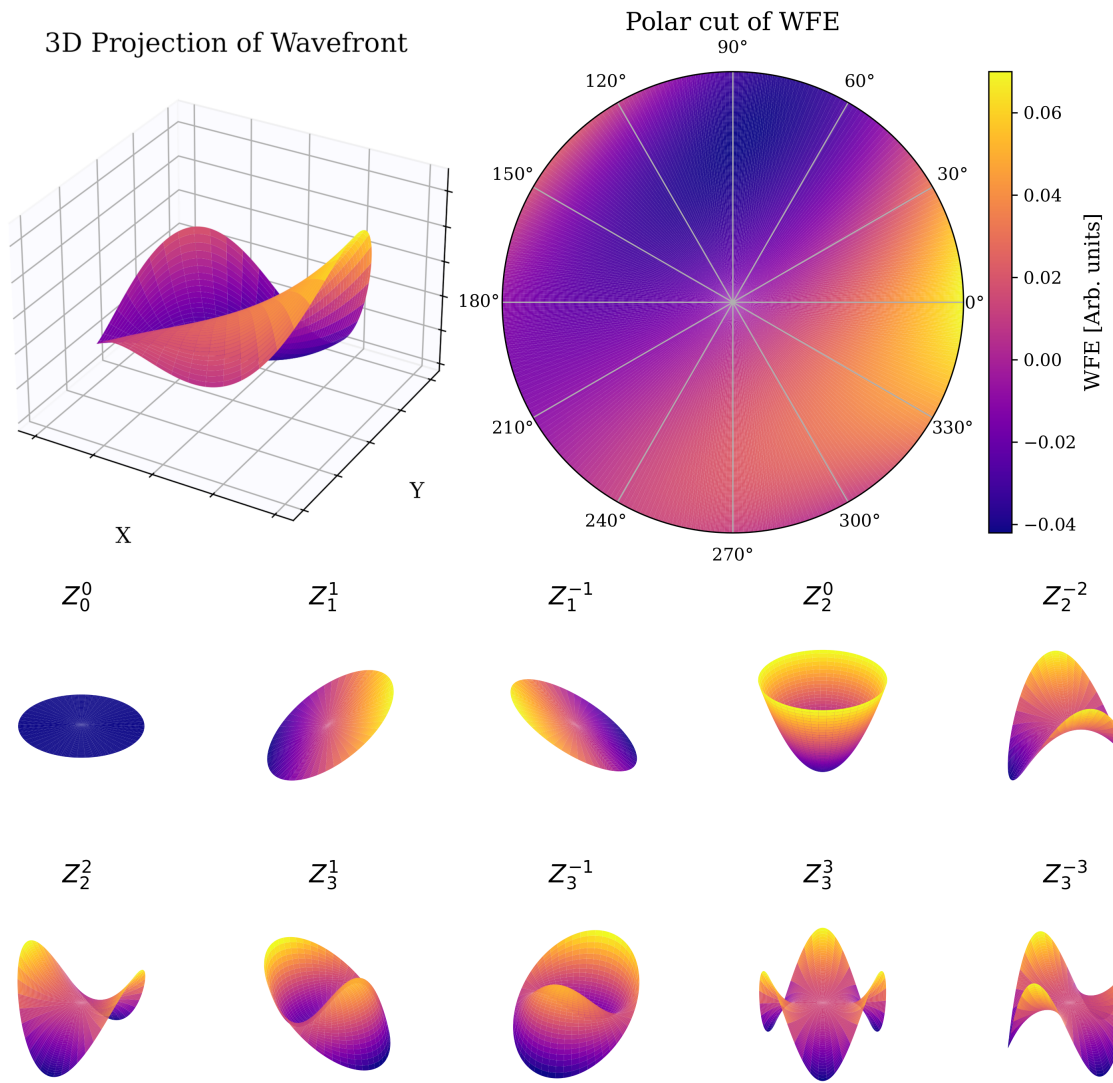


Figure 1.2 Simulation of a wavefront employing all Zernikes with  $n \leq 3$ . The top left panel shows the 3-dimensional representation of the wavefront and the top right panel shows a cut in a plane normal to the direction of travel. The bottom two rows show the shape of the individual Zernike polynomials included in the simulation.

The algorithm works by minimizing a cost function that depends on the OTF of the system which can be parametrized by the Zernike expansion (Paxman et al., 1992):

$$\mathcal{L}(C) = \sum_k \frac{|\hat{I}_1(\nu)\hat{S}_2(\nu, C) - \hat{I}_2(u)\hat{S}_1(\nu, C)|^2}{|\hat{S}_1(\nu, C)|^2 + |\hat{S}_2(\nu, C)|^2}, \quad (1.10)$$

where k represents the pairs of aberrated (subindex 1) and unaberrated (subindex 2) images, I stands for the intensity distributions, and S for the system's OTF expressed in terms of a Zernike expansion with coefficients C.

By finding the coefficients of the zernike expansion that minimize  $\mathcal{L}$ , we are able to characterize the wavefront and identify the aberrations present in the optical system. Thus, determining the OTF, and consequently the PSF.

Our interest in determining the wavefront and OTF is not only to evaluate the instrument's performance but also to enable image restoration by mitigating the aberrations introduced during the imaging process. The procedure for removing the effects of the aberrations consists on removing the influence of the PSF on the final intensity distribution. In other words, the goal is to *deconvolve* the PSF from the image.

Coming back to equation (1.1), we can simplify the integrals to a convolution operator assuming an spatial invariance of the PSF. In that case, the observed intensity can be expressed by:

$$I(\xi, \eta) = O(\xi, \eta) * S(\xi, \eta) + N(\xi, \eta) \quad (1.11)$$

where we added a term accounting for the noise present in real measurements  $N(\xi, \eta)$ .

The treatment of the problem is easier in the Fourier domain, where the convolution operator becomes a product of the fourier transforms of the corresponding functions. Therefore, in the Fourier domain, eq. 1.11 becomes:

$$\hat{I}(\nu) = \hat{O}(\nu)\hat{S}(\nu) + \hat{N}(\nu), \quad (1.12)$$

Since neither  $\hat{O}(\nu)$  nor  $\hat{N}(\nu)$  are known, it is not possible to analytically derive the object, even if the system's response, is known. Therefore, statistical approaches must be employed to deconvolve PSF.

One such approach is the Wiener-Helstrom filter (Helstrom, 1967), which proposes that the estimated object,  $\tilde{O}$ , can be computed as:

$$\tilde{O}(\nu) = \frac{\hat{S}^*(\nu)\hat{I}(\nu)}{|\hat{S}(\nu)|^2 + P_N(\nu)/P_O(\nu)}, \quad (1.13)$$

where the term  $P_N(\nu)/P_O(\nu)$  represents the ratio between the power spectral densities of the noise and the object. Although this factor is unknown, it can be estimated based on the expected S/N in the data.

### 1.4.2 Spectroscopy

Among the tunable filtergraphs, Fabry-Pérot Interferometers (FPIs), also known as etalons (used interchangeably), represent one of the most prevalent forms of narrow-band tunable spectrographs. Composed by a resonant optical cavity formed by two distinct optical media, these devices allow only the passage of light with wavelengths corresponding to constructive interference within the cavity.

The transmission profile of an etalon, being produced by an interference phenomenon, is characterized by a series of narrow and periodic transmission peaks. The wavelengths at which these resonance peaks are located, their width, and their separation are determined solely by the physical properties of the etalon. In fact, it is not difficult to demonstrate (Bailén et al., 2019) that a resonant cavity produces a periodic transmission profile, with maxima occurring at a wavelength  $\lambda$  such that:

$$\lambda = \frac{2nd \cos \theta}{m}, \quad (1.14)$$

where  $n$  is the refractive index of the medium inside the cavity,  $d$  is the distance between the mirrors,  $\theta$  is the angle of incidence of the incoming light ray and  $m$  is the interferential order ( $m \in \mathbb{Z}$ ).

With Eq. (1.14) in mind, it is clear that an etalon allows for tuning the wavelengths of the transmission peaks by either changing the distance between the mirrors or by altering the refractive index. Although changing the angle of incidence also results in a wavelength shift, it introduces other issues, such as ghost images or profile broadening in telecentric configurations, among other effects. Consequently, the angle is not used for wavelength tuning.

To isolate a single wavelength, or a narrow band surrounding it, it is necessary to select one transmission peak, often referred to as the main order. This is typically achieved by using a pre-filter with a small bandwidth that only allows light with wavelengths near the desired measurement region to pass through. This prefilter prevents light from other interference orders than the main one, known as secondary orders, to reach the instrument.

Figure 1.3 shows a simulation of the spectral behavior of this optical setup. The order-sorting pre-filter is shown with a shaded purple area and the unaltered transmission profile of the etalon is shown in dashed lines for different values of the refractive index. In solid lines, the resulting transmission profile is shown, that is, the transmission allowed through both the pre-filter and etalon at the same time.

### 1.4.3 Polarimetry

A polarimeter must determine the full Stokes components of the incoming light; however, these properties cannot be directly measured, as only the intensity of light is observed, not its intrinsic characteristics. Thus, polarimeters derive the Stokes parameters, rather than measure them. In order to do so, a series of multiple, simultaneous or quasi-simultaneous observations are taken, in which the polarization state of the incoming light is systemat-

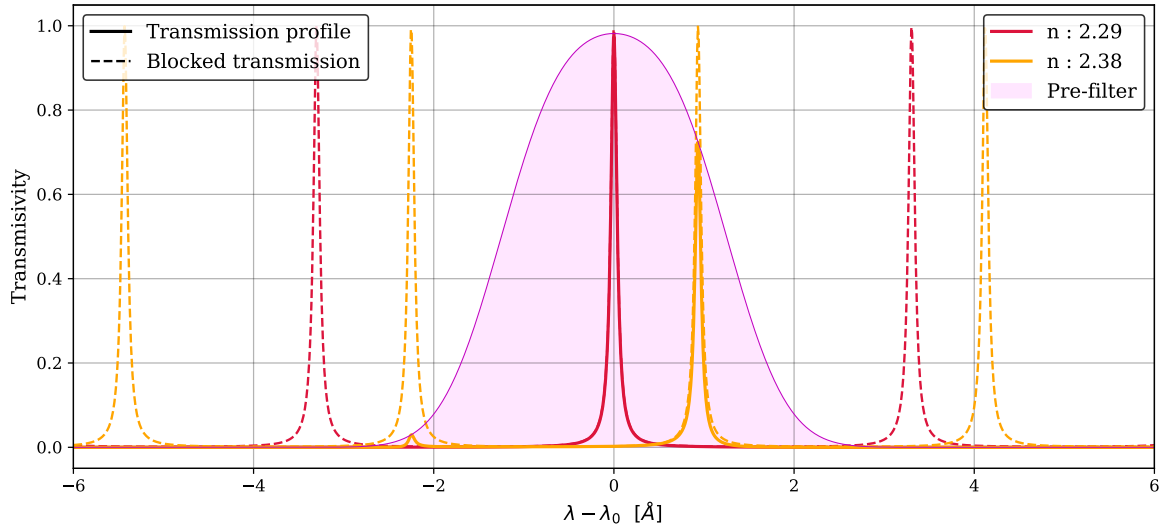


Figure 1.3 Transmission profiles of the same etalon with varying refractive indices (n). The dashed lines represent the original transmission profile, while the solid lines indicate the portion of the transmission profile that passes through the order-sorting pre-filter (shaded purple area).

ically altered. These different measurements, commonly referred to as modulations, are generated by inducing a known alteration in the polarization. The Stokes parameters are then reconstructed by combining the information from all measurements through a process known as demodulation.

In order to understand how polarimeters derive the stokes components we need to briefly model how the different modulations are generated. Mathematically, the effect on polarization of a linear and finite system can be treated as a combination of linear transformations on the Stokes vector and, therefore, can be represented by a matrix in  $\mathbb{R}^4$ , known as the *Mueller Matrix*. Let  $\mathbf{M}$  be the matrix that describes these transformations, then the polarization state that reaches the detector follows:

$$\mathbf{I}_{out} = \mathbf{M}\mathbf{I}_{in}, \quad (1.15)$$

where  $\mathbf{I}_{in}$  and  $\mathbf{I}_{out}$  are the Stokes vectors of the light that reaches the instrument, and the detector, respectively. However, since we only measure intensities, the actual quantity measured by our CCD is:

$$I_{obs} = m_{00}I_{in} + m_{01}Q_{in} + m_{02}U_{in} + m_{03}V_{in} , \quad (1.16)$$

where  $m_{0i}$  is the i-th element of the first row of the Mueller Matrix. This means that the intensity we measure is a linear combination of the different polarization states of the incoming light. To determine the values of the individual parameters  $I_{in}$ ,  $Q_{in}$ ,  $U_{in}$ , and  $V_{in}$ , further independent measurements are necessary, which can be achieved by modifying the Mueller matrix. In particular, it is easy to see that four independent measurements are re-

quired in order to construct a system of equations that allows us to determine the full Stokes vector. This process is known as modulation, and the four independent measurements are the different modulations.

If we denote each of the modulations by  $I_j$  with  $j \in \{1, 2, 3, 4\}$ , we can construct the following system of equations:

$$\begin{pmatrix} I_1 \\ I_2 \\ I_3 \\ I_4 \end{pmatrix} = \underbrace{\begin{pmatrix} m_{01}^1 & m_{02}^1 & m_{03}^1 & m_{04}^1 \\ m_{01}^2 & m_{02}^2 & m_{03}^2 & m_{04}^2 \\ m_{01}^3 & m_{02}^3 & m_{03}^3 & m_{04}^3 \\ m_{01}^4 & m_{02}^4 & m_{03}^4 & m_{04}^4 \end{pmatrix}}_{\mathbf{O}} \begin{pmatrix} I_{in} \\ U_{in} \\ Q_{in} \\ V_{in} \end{pmatrix} \quad (1.17)$$

where the superindex in  $m_{oi}^j$  denotes the values of the Mueller Matrix for each modulation. Through straightforward algebra, it is easy to see that the stokes vector of the incoming light can be determined by  $\mathbf{I}_{in} = \mathbf{D}\mathbf{I}_{obs}$ , where  $\mathbf{D}$  is the demodulation matrix, the inverse of the modulation matrix,  $\mathbf{O}$ , and  $\mathbf{I}_{obs}$  is the vector containing the 4 measured modulations.

Carefully determining  $\mathbf{O}$ , and consequently  $\mathbf{D}$ , during the instrument calibration process is crucial, as the accuracy of the determination of the Stokes components depends entirely upon it. It can be proven (del Toro Iniesta & Collados, 2000) that the optimum modulation scheme—the values of  $\mathbf{D}$  that enable the Stokes vector to be computed with minimal uncertainty—satisfies the conditions:

$$\varepsilon_1 \leq 1, \text{ and } \sum_{i=2}^4 \varepsilon_i^2 \leq 1, \quad (1.18)$$

where the polarimetric efficiencies for each stokes parameter ( $i = 1, 2, 3, 4$ ),  $\varepsilon_i$ , are defined as:

$$\varepsilon_i = \left( N_p \sum_{j=1}^{N_p} D_{i,j}^2 \right)^{-1/2}, \quad (1.19)$$

where  $N_p$  is the number of independend modulations.

When designing the modulation scheme for a given instrument, it is essential to satisfy the efficiency conditions given in Equation (1.18) to ensure optimal polarimetric accuracy for all Stokes components. Furthermore, for equal sensitivities in the measurements of Stokes parameters Q, U, and V, the corresponding efficiencies should all be equal, with a value of  $1/\sqrt{3}$ . This is a very important result beacause polarimetric efficiencies are directly related to the smallest measurable polarimetric signals, the polarimetric sensitivity—essentially the inverse of the signal-to-noise ratio (SNR). This relation can be expressed as (del Toro Iniesta & Collados, 2000):

$$\left( \frac{S}{N} \right)_i = \frac{\varepsilon_i}{\varepsilon_1} \left( \frac{S}{N} \right)_1, \quad i = 2, 3, 4. \quad (1.20)$$

From equations (1.20) and (1.18) it is clear that the sensitivities for computing Stokes Q, U, and V will always be lower than that of Stokes I, as their corresponding efficiencies are

smaller. To achieve an SNR of  $10^3$  in Stokes measurements, which is the sensitivity required to detect weak polarization signals, an SNR of at least  $(S/N)_0 \gtrsim 1700$  is necessary in the measurement of Stokes I for a quasi-optimal modulation scheme.

Spectropolarimeters ultimately combine measurements in polarization, spectral, and spatial (image) domains. Consequently, the final observed intensity depends on all three properties simultaneously. By integrating the spectral behavior of the etalon and pre-filter with the polarimetric measurements, and taking into account the spatial dependence of these measurements, we can revisit equation (1.1) and rewrite it for FPI-based spectropolarimeters. In that case, the observed intensity for a modulation  $j$  at any point of the focal plane  $\eta, \xi$  when the etalon is tuned at a wavelength  $\lambda_s$  is determined by:

$$I_j(\xi, \eta; \lambda_s) = g(\xi, \eta) \int_0^\infty T(\lambda) \iint O_j(\xi_0, \eta_0; \lambda) S(\xi_0, \eta_0; \xi, \eta; \lambda - \lambda_s) d\xi_0 d\eta_0 d\lambda, \quad (1.21)$$

where  $T(\lambda)$  accounts for the presence of the order-sorting pre-filter,  $S(\xi_0, \eta_0; \xi, \eta; \lambda - \lambda_s)$  accounts for the imaging response of the instrument when the etalon is tuned at the wavelength  $\lambda_s$ ,  $g(\xi, \eta)$  represents a spatial gain factor that accounts for any wavelength independent pixel-to-pixel intensity fluctuations occurring in the focal plane, and  $O_j(\xi_0, \eta_0; \lambda)$  is the intensity distribution of the incoming light for a modulation  $j$  and is given by:

$$O_j(\xi_0, \eta_0; \lambda) = m_{00}^j I_{in}(\xi_0, \eta_0; \lambda) + m_{01}^j Q_{in}(\xi_0, \eta_0; \lambda) + m_{02}^j U_{in}(\xi_0, \eta_0; \lambda) + m_{03}^j V_{in}(\xi_0, \eta_0; \lambda) \quad (1.22)$$

#### 1.4.4 What do spectrpolarimeters tell us about the Sun?

Spectropolarimeters are often referred to as magnetographs (e.g., TuMag), suggesting they measure magnetic fields directly. However, this is not entirely accurate. In astrophysics, the physical properties of the light source are inferred by correlating them with the observed properties of the light, rather than measuring them directly. By evaluating the polarization of sunlight at different wavelengths, spectropolarimeters enable us to infer the magnetic field and estimate plasma velocities on the solar surface.

The simplest calculation we can carry out that provides us with physical quantities of the Sun is that of the line-of-sight (LOS) velocities. Given the spectral shift of a specific absorption or emission spectral line,  $\Delta\lambda$ , with respect to its rest position,  $\lambda_0$ , the LOS velocities can be computed with the Doppler formula:

$$v_{\text{LOS}} = \frac{\Delta\lambda}{\lambda_0} c, \quad (1.23)$$

where  $c$  stands for the speed of light in vacuum.

The polarization properties of light come into play when determining the magnetic fields. Due to Zeeman and Hanle effects, the polarity and spetcroscopy of spectral lines can be altered when formed in the presence of magnetic fields. Due to the Zeeman effect, the spectral lines widen or split into different polarized components when a strong magnetic

field is present (del Toro Iniesta, 2003), such as in the surroundings of sunspots and active regions. In the other hand, the Hanle effect is sensitive to weaker fields, and can be used to study, for example, the magnetic structure of solar prominences or turbulent fields in the solar photosphere (Bianda et al., 1998) where the fields are not strong enough to leave an imprint through the Zeeman effect.

One simple strategy to employ polarization and spectral data to derive the magnetic fields is through the center-of-gravity method. According to Uitenbroek (2003), the LOS strength of the magnetic field can be obtained through:

$$B_{\text{LOS}} = \frac{\lambda_+ - \lambda_-}{2} \frac{4\pi mc}{eg_L \lambda^2} , \quad (1.24)$$

where  $m$  and  $e$  are the electron mass and charge respectively,  $g_L$  stands for the Landé factor and  $\lambda_+$  and  $\lambda_-$  are the centroids of the right and left circularly polarized line components, respectively, and are computed by:

$$\lambda_{\pm} = \frac{\int \lambda [I_{\text{cont}} - (I \pm V)] d\lambda}{\int [I_{\text{cont}} - (I \pm V)] d\lambda} , \quad (1.25)$$

where the subindex "cont" stands for the wavelength at the continuum.

The vector magnetic field (*i.e.*, strength, azimuth and inclination), and not only the LOS strength can also be derived. However, the derivation of these quantities has to be achieved through inversions of the radiative transfer equation (RTE). The applicability of the different methods to carry out this inversion is an extensive topic as there are some assumptions that can be applied in some cases but not in others, such as the weak-field or Milne-Eddington approximations, among others. For an extended discussion of this topic, we refer the interested reader to del Toro Iniesta & Ruiz Cobo (2016).



## CHAPTER 2

---

### TUMAG'S PIPELINE AND DATA.

The 2024 observational campaign of the third edition of the Sunrise observatory was an outstanding success. In contrast to previous flights, where technical challenges severely limited the number of useful observations, all subsystems performed exceptionally well during this third flight, allowing for nearly continuous instrument operation over more than six days. From TuMag's perspective, the campaign yielded approximately 10 terabytes of data, consisting of over 40 scientific observation blocks and 250 calibration observations.

The substantial volume of data recorded by the three instruments, of which TuMag captured the least (in digital space) due to the instrument's nature, required that it be physically recovered on-site, as it could not be broadcasted from the observatory to the operations center. Recovery activities began immediately after landing and lasted until early August, during which all surviving components, along with the data vaults, were transported to Yellowknife, Canada, the nearest city to the landing site. The data vaults arrived at MPS in early August, where a backup was created before the data associated with each instrument was sent to the respective IP institution. TuMag's data arrived at IAA in late August, marking the official start of the reduction process.

The reduction process began by labeling all images and identifying the more than 600 000 images captured by TuMag. Once the observations were correctly identified, the reduction process commenced and, at the time of writing, remains ongoing. Due to the relevance of the pipeline development and results for this thesis, this chapter will provide an overview of TuMag's data and the state of its pipeline, although the results remain preliminary.

The discussion will begin by introducing TuMag's various observing modes, both scientific and calibration, followed by a brief review of the observation campaign, outlining the different observation programs and their scientific objectives. The chapter will conclude with an examination of the data reduction process, detailing the pipeline and presenting some initial results. It is important to note that, due to the late arrival of the data, this thesis had to be written in parallel with the reduction process. Therefore, the results presented here are preliminary, and the final product may differ as additional reduction steps are incorporated.

Observing mode	Spectral lines	$N_\lambda$	$N_P$	$N_a$	$N_c$	$t_{eff}(s)$	(S/N)
0s	Mg I $b_2$ 5172.7 Å	12	1	2	1	6.3	500
0p	Mg I $b_2$ 5172.7 Å	12	4	16	1	37.62	1000
1	Mg I $b_2$ 5172.7 Å	10	4	16	1	31.81	1000
2	Fe I 5250.2 Å, Fe I 5250.6 Å	8	4	16	1	23.4	1000
3	Fe I 5250.2 Å, Fe I 5250.6 Å	5	2	20	1	10.04	1000
4	Mg I $b_2$ 5172.7 Å	3	4	10	10	54.01	2500
5	Fe I 5250.2 Å, Fe I 5250.6 Å	3	4	10	10	53.60	2500

Table 2.1 Scientific observing modes. From left to right, the columns are: observing mode identifier, measured spectral lines, number of wavelengths, of modulations, of accumulations, of cycles, the total time and the polarimetric SNR.

## 2.1 TuMag's observing modes

With the purpose of simplifying the operation activities, TuMag operates through a series of so-called observing modes. The observing modes are a list of pre-configured settings tailored for various observations, including both calibration and scientific purposes. Each mode is designed to fulfill the specific objectives of the corresponding observation and enables nearly automatic operation of the instrument during flight.

A summary of the properties for each observing mode is provided in Table 2.1. There are four distinct modes designed to observe the magnesium line. Mode 0s performs a fast, extended scan of the spectral line using 12 wavelength samples: [-40, -30, -20, -10, 0, 10, 20, 30, 40, 50, 60, 65]\*, with one modulation and two accumulations to maximize scanning speed. Mode 0p is similar to mode 0s but employs a full-vector modulation scheme, requiring 16 accumulations to ensure the required SNR. Mode 1 provides a shortened scan of the magnesium line, with measurements taken at [-30, -20, -10, -5, 0, 5, 10, 20, 30, 65], also utilizing a vectorial modulation scheme. Finally, mode 4 is a "deep" magnetic mode, featuring a highly reduced scan with only three samples at [-10, 0, 10], but with increased accumulations and cycles to enhance polarimetric sensitivity.

Three observing modes are configured for the iron lines. Mode 2 employs a vectorial modulation scheme applicable to both iron lines, with sampling at [-12, -8, -4, 0, 4, 8, 12, 22] pm. Mode 3 uses a longitudinal modulation scheme, measuring only Stokes I and V, with samples taken at [-8, -4, 4, 8, 22] pm. Lastly, mode 5 closely resembles mode 4, but is configured for the iron lines, with sampling at [-8, 0, 8] pm. The only difference between these two modes is the sampling scheme.

Although most of the parameters are set up by the observing mode and cannot be changed, there are some configurable parameters that allow to slightly modify the observing modes to fit the specific goal of a particular. These parameters are the following:

Solo estos? o había más?

- ✿  $\lambda_{rep}$  : A parameter that allows to repeat all the observations carried out at every

\*Sampling positions are given relative to the line core.

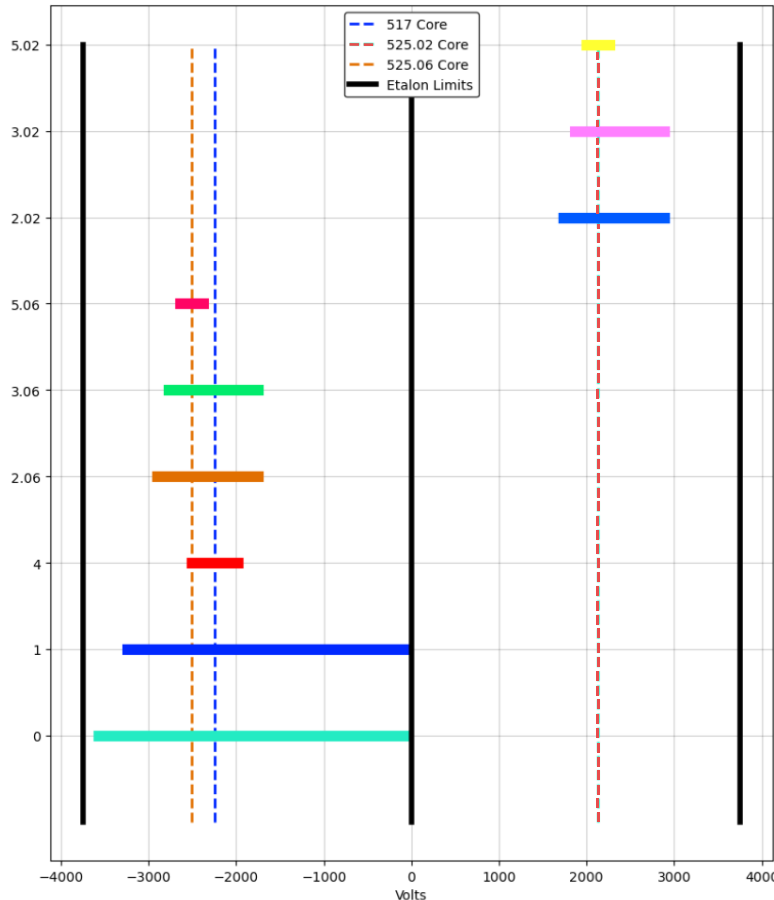


Figure 2.1 Schematic representation of the voltage range covered by all observing modes. The dashed lines indicate the position of the line core as measured during the E2E tests performed at INTA in December 2021. The black lines represent the voltage limits that cannot be crossed in an observing mode.

spectral position before changing wavelength. This parameter is employed for flat-field observations (see the following section). By default is set to 1.

- Etalon offset : A parameter that allows for the introduction of a global shift to the spectral sampling by offsetting the absolute voltages (and thus, wavelengths) of the scan. This parameter was used to center the spectral line in shorter observing modes affected by solar rotation or other effects that might shift the spectral position. The default value is set to 0 V.
- $N_a$  : Even though the number of accumulations is fixed in nominal observing modes, this parameter was set as configurable in order to allow modifications for faster observations when needed. The default value depends on the observing mode.

Figure 2.1 presents a schematic representation of the voltage ranges for the observing modes when converting spectral sampling to volts. The black lines indicate the voltage boundaries that cannot be surpassed during an observation due to technical constraints. These limits are set at  $\pm 3750$  V as the maximum and minimum values, with an additional limitation at 0 V, since a polarity change poses technical challenges that could not be addressed within an observation mode. These restrictions are significant in two cases: firstly,

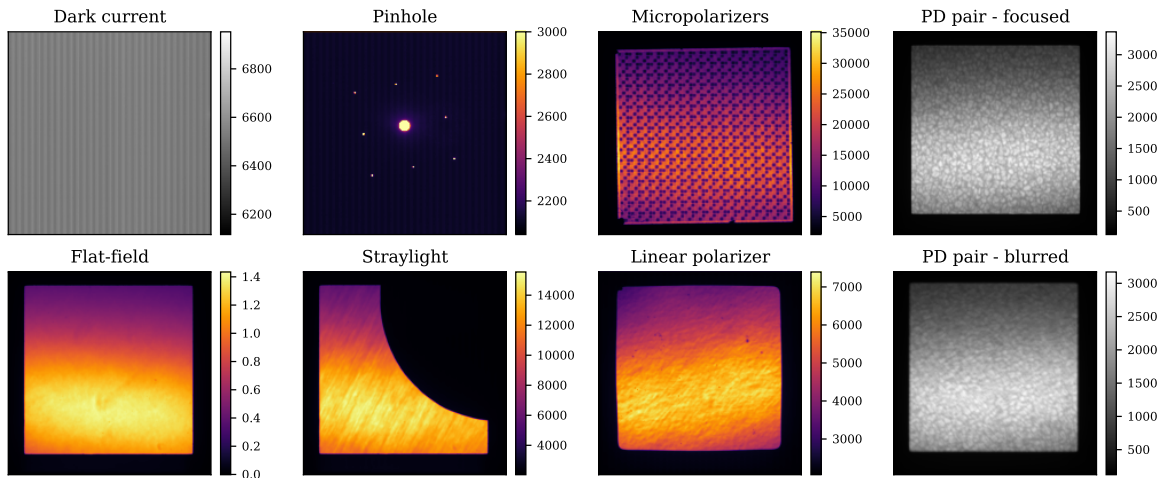


Figure 2.2 Examples of calibration observations. All images, with the exception of the flat-field, are presented in their raw format, without any manipulation or correction applied. The flat-field observation depicted corresponds to the first modulation of the continuum measurement obtained during a flat-field observation corresponding to observing mode 1. All data are belong to camera 1, and the colorbar is calibrated in digital counts save for the flat-field which is normalized to its mean value.

for Magnesium observation modes, specifically modes 1 and 0, where the continuum measurement is positioned as far from the core as possible, at -80 V, due to the 0 V crossing limitation. Secondly, these constraints are relevant when applying an etalon offset to shift the spectral positions of a particular observing mode, as the offset cannot cause the final positions to exceed these boundaries.

### 2.1.1 Calibration modes

An additional type of observing modes are also designed aimed at carrying out calibration observations. These calibration observing modes are more flexible than scientific ones, and allow for the configuration of several parameters to match the observations to the aim of the scientific observation.

#### 2.1.1.1 Flat-field observations

One of the essential calibration procedures in any telescope-based astronomical observation is the acquisition of flat-field images. These observations are designed to measure intensity variations across the FoV, which arise from several factors, including intensity gradients induced by the etalon, dust particles, or pixel efficiency variations, among other sources. The aim is to capture a region with no discernible structure, ideally producing a uniformly flat intensity distribution. However, achieving such flat-field observations is not always straightforward, particularly for certain instruments. While ground-based tele-

scopes can utilize twilight periods to observe areas of the sky devoid of stars, space-borne or balloon-borne solar telescopes, such as Sunrise III, are unable to the same and must look for alternative methods.

In Sunrise III, flat-field images are generated by deliberately blurring the solar image through rapid movements of the mirror. This process effectively removes any solar structure from the FoV when averaging out multiple blurred observations, resulting in a flat-field image devoid of solar features.

In the case of TuMag, flat-field observations are performed using a modified version of the nominal observing mode, where the  $\lambda_{\text{rep}}$  is set to 4. Additionally, multiple consecutive instances ( $N_{\text{reps}}$ ) of these observations are executed, typically 5 or 7. During data processing, a single flat-field is generated for each wavelength position and modulation state by averaging all corresponding observations.

Figure 2.2 shows an example of a flat-field observation, for one camera, modulation and wavelength (bottom left panel). The image shows a clear deviation from flatness in the measurement, primarily due to the etalon intensity gradient, which accounts for the change in intensity between the brighter bottom half and the darker top half, and some minor inhomogeneities over the FoV.

### 2.1.1.2 Dark-current observations

A second critical calibration procedure for any observation involving electronic cameras is the measurement of dark current. In the absence of incident photons, electrons within the camera's wells can still be randomly excited. This spontaneous excitation can be incorrectly interpreted as photon-induced counts when analyzing the data. Dark current observations are designed to characterize these random electronic excitations, which are primarily influenced by the camera's physical conditions, particularly temperature, so that they can be accurately subtracted from the final images.

For TuMag, dark current calibration involved capturing a series of 50 images with  $N_a = 50$  with no light entering the instrument. As with flat-field observations, a single dark current frame for each camera is generated by averaging all individual observations. In the top left panel of fig. 2.2 a dark current shot is depicted, characterized by the vertical strips pattern.

### 2.1.1.3 Linear polarizer and micropolarizers observations.

TuMag's filter wheels are equipped with two targets designed to assess the instrument's polarimetric performance: a linear polarizer and a set of micropolarizers. Both targets are situated in the first filter wheel and are used in conjunction with the three distinct prefilters located in the second filter wheel. The linear polarizer serves to evaluate the polarimetric calibration, particularly by quantifying the level of cross-talk, as no circular polarization should be detected when using this target. The micropolarizers provide a more complete assessment, as they consist of multiple linear polarizers oriented at different angles.

Observations with this targets are carried with the three prefilters, at a single wavelength, located in the continuum of each line. For each measurement, a vectorial modula-

tion scheme is employed that allows for the derivation of the four stokes parameters. In the third column of figure 2.2 observations of both targets are shown.

#### 2.1.1.4 Pinhole Observations.

Another calibration target included in the filter wheels is the pinhole target. This target blocks most of the light reaching the instrument, except for a few small holes arranged in a square-like pattern across the FoV, as shown in the top panel of the second column of figure 2.2. A larger hole is located at the center of the FoV, surrounded by eight smaller holes that trace a square with the central hole at its midpoint. These observations serve various purposes, including image alignment, detecting the presence of ghost images, or identifying etalon reflections, among other uses.

Pinhole observations are conducted similarly to those with polarizers, that is, in combination with the three prefilters at a single wavelength (the continuum of each line), but without applying any modulation.

#### 2.1.1.5 Straylight target.

Not all the light that reaches the detector is necessarily the intended signal for a given observation. Some unwanted light, primarily originating from internal reflections along the optical path, may also reach the instrument. This unwanted contribution, known as straylight, contaminates the measurements by reducing contrast, lowering the S/N, and generally degrading the spectral, optical, and polarimetric performance of the instrument.

To address this contamination, TuMag performed a series of observations using a target that blocks part of the FoV (see the bottom panel of the second column of figure 2.2). By analyzing the dark region in these observations, it becomes possible to measure and model the straylight reaching the instrument, allowing for its subsequent removal from the data.

#### 2.1.1.6 Prefilter scans.

TuMag observations are very sensible to spectral shifts either from the pre-filters or from the observed spectral line position. The shift of the pre-filters can happen due to changes in the physical conditions of the filter wheels such as changes in temperatures which spectrally shift the behavior of the pre-filters. The position of the pre-filter greatly affect the measurements as it reduces the intensity of the measurements that are obtained in the wings of the pre-filter. Due to solar rotation, or changes in the conditions of the etalon, although these are less likely, the spectral position at which the spectral lines are recorded can change. This effect is specially important in observing modes that require great spectral accuracy, such as the deep modes, where only three spectral positions close to the line core are employed.

In order to verify the spectral behaviour of the prefilter, as well as the position of the spectral line, a series of observations were carried out, usually before and after the scientific observations, where a spectral scan with a rich spectral smapling was taken for all the pre-filters employed in the observation. These scans, measure the voltage range of the specific line with a sampling of 100V and without modulating.

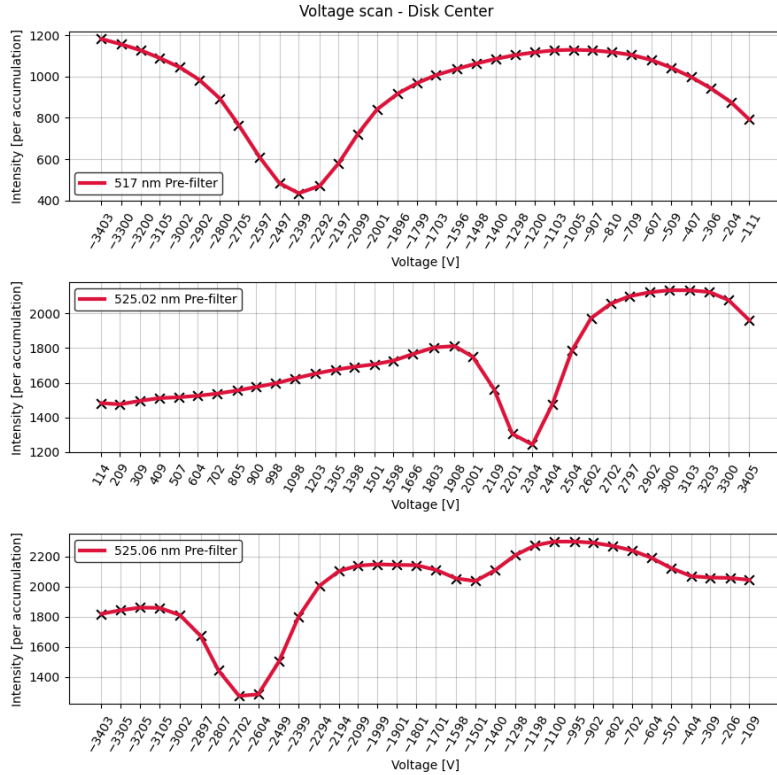


Figure 2.3 Schematic representation of the voltage range covered by all observing modes. The dashed lines indicate the position of the line core as measured during the E2E tests performed at INTA in December 2021. The black lines represent the voltage limits that cannot be crossed in an observing mode.

### 2.1.1.7 Phase diversity.

Lastly, TuMag is equipped with the capability to perform phase diversity for image reconstruction. As discussed in previous chapters, applying image reconstruction techniques is essential to meet the optical quality requirements. To this end, TuMag includes a PD plate in the first filter wheel that introduces a known defocus in the images. Capturing images with and without this plate enables the computation of the instrument's PSF, which can then be deconvolved from the data.

PD measurements require quasi-simultaneous pairs of aberrated and unaberrated images. Therefore, TuMag's PD observations consist of a series of 32 or 40 rapid, non-accumulated shots with the PD plate, followed by a corresponding series without the PD plate. The feasibility of this sequential scheme for phase diversity techniques has been confirmed in Bailén et al. (2022). A pair of focused-defocused images of quiet-sun observations is shown in the last column of figure 2.2.

## 2.2 Timelines

The operations of Sunrise III were designed to be nearly autonomous to ensure synchronization between the scientific instruments, the telescope, and the CWS. Given the limited time available for the observation campaign, this autonomy also helps to speed up operations, thus enabling more observation programs to be accommodated within the mission's

duration.

The Sun is a highly dynamic system, exhibiting a wide range of behaviors and phenomena, from large-scale structures such as active regions, sunspots, and flares, to smaller, quiet Sun structures where interactions at small scales drive the evolution of magnetic flux. This diversity, observable in various spectral lines and across different regions of the solar disk, demands multiple observations with distinct characteristics.

Prior to the first flight of Sunrise III in 2022, a series of timelines were developed to program both calibration and scientific observation blocks. These timelines were carefully designed by the Sunrise Science Team, taking into account the 70 observing proposals submitted for Sunrise, in order to prioritize observations that met the requirements of the majority of these proposals.

Observing proposals that could be fulfilled by targeting the same solar feature, while considering its disk position, were grouped into a single timeline. Each timeline included not only the necessary scientific observation blocks but also the required calibration observations to ensure data accuracy. Thus, timelines consist of a sequence of scientific and calibration observation blocks. The observing blocks within a timeline could vary in content depending on the scientific objectives and the status of the other instruments involved.

For simplicity, operations related to SCIP and SUSI will be excluded from the discussion, save for a few important remarks. In the case of TuMag, each observing block was composed either of a combination of two observing modes executed consecutively, or a single observing mode repeated throughout the block.

The timelines of the Sunrise III observation campaign can be grouped in the following blocks:

- ✿ Quiet Sun observations at disk center (QSDC), as the name implies, focus in regions near the solar disk center that are free from significant solar activity. These timelines typically involve long series of observations aimed at studying the small-scale structure and magnetic flux evolution in the quiet Sun.

There are four distinct timelines in this category: three standard timelines, which employ the nominal observing modes, and a different timeline, the (QSDC\_HC). This timeline employs high-cadence variations of the standard observing modes specifically designed to enhance the temporal resolution between images, which is crucial for helioseismology techniques.

- ✿ Sunspot observations (SP) are specifically designed to study sunspots. There are four different timelines for this purpose. Some of these are short programs used to track the same sunspot over multiple days, with the goal of studying the evolution and decay of the sunspot. Others are more extensive programs aimed at examining, in greater detail, the magnetic activity of sunspots and their penumbral structures.
- ✿ Polar observations (PL) target the region close to the limb in both poles of the Sun. These areas are of special interest due to their distinct magnetic behavior compared to the disk center. Additionally, these regions provide the opportunity to measure faint signals outside the main solar disk, such as spicules in the lower chromosphere,

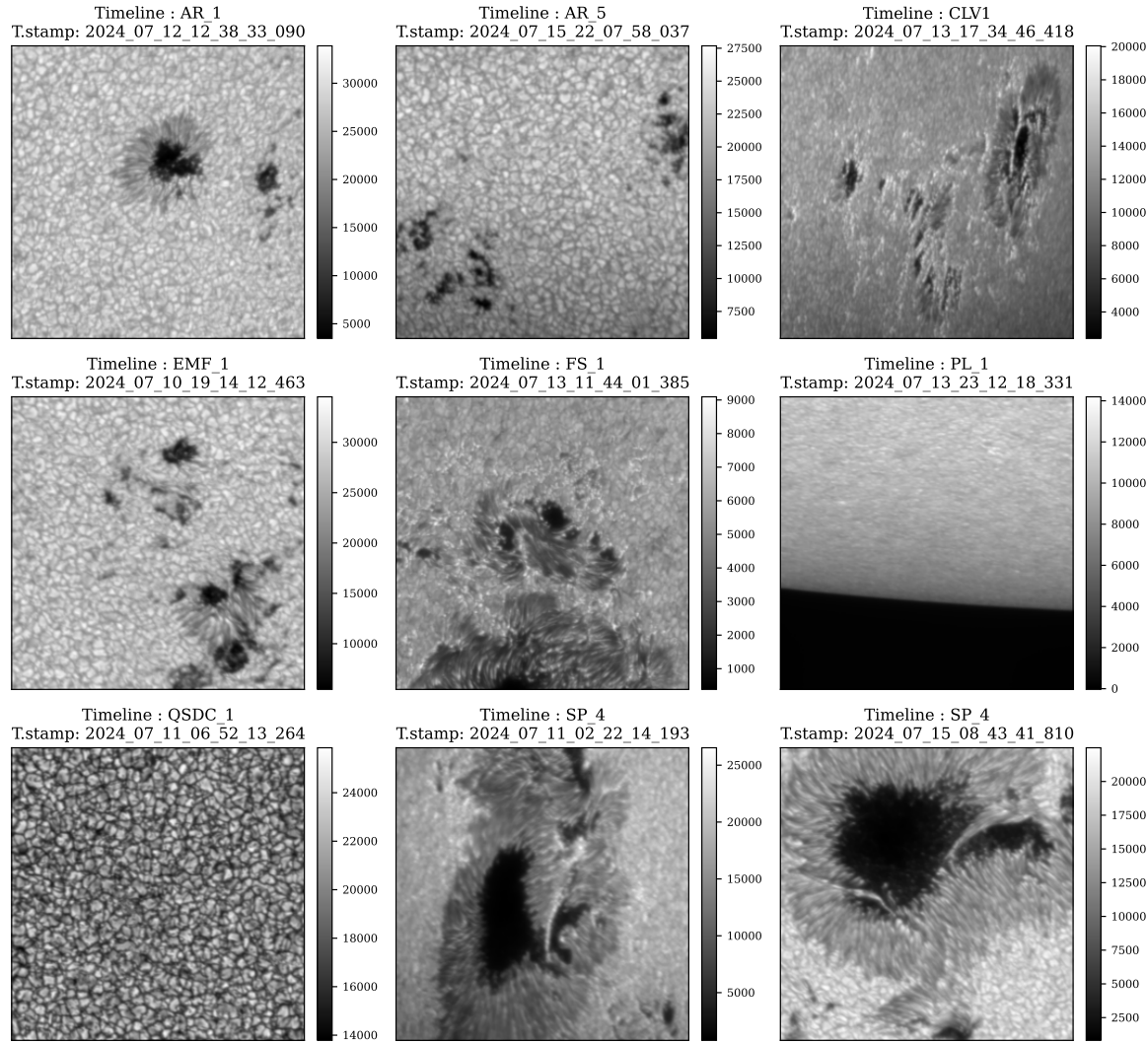


Figure 2.4 Continuum images of the first modulation of the first observation mode from different timelines. The image shown has been flat-fielded and dark-corrected. The timestamp provided corresponds to the first image of the observation mode. The colorbar is given in counts.

observed outside the continuum disk of iron. Two different instances of these timelines are conceived in the observation campaign, mostly differentiated in TuMag by the selected spectral lines.

- East and West limb (EW) observations are designed to target the equatorial regions of the solar limb. In addition to exhibiting magnetic structures distinctly different from those observed at the poles, the reason for having a separate timeline from the PL timelines lies in the orientation and technical constraints related to SCIP and SUSI's slits. The relative positioning of the regions and the inclination of the telescope introduce unique challenges. In these EW observations, the spectrometer slits are aligned parallel to the limb, contrasting with the PL timelines, where the slit is positioned perpendicular to the limb.
- Active regions (AR) observations are designed to study areas exhibiting solar activity, excluding those specifically focused on in the sunspot programs. These observations typically consist of two-hour series, employing the standard combination of the iron 525.02 nm and magnesium lines, using modes 1 and 2.02, which represent the most common observation block for TuMag. Although five different AR timelines were planned for the Sunrise campaign, only three were executed.
- Emergence flux (EMF) programs are specifically designed to study active regions that exhibit a large flux emergence. For TuMag, the observation blocks are shared with those of the AR programs, namely, the combination of mode 1 and 2.02 for series of around 2 hours.
- Full spectral scan (FS) observations are primarily designed for SUSI and SCIP, where their complete set of spectral bands is utilized. These scans are intended to be carried out in both quiet Sun and active regions. For TuMag, FS observations consist of long series focusing on the iron spectral line in quiet Sun regions, while in active regions, they include a combination of iron and magnesium observations.
- The flares programs (FL) were designed for target opportunities of a flaring region. These programs were intended to be activated only when an active region showed signs of flaring. For TuMag, the observations during these programs consist of the standard combination of iron 525.02 nm and magnesium spectral lines.
- Center-to-limb variation (CLV) observations were intended to target regions of the solar disk characterized by  $\mu$  values that had not been previously observed. The parameter  $\mu$ , defined as the cosine of the angle between the surface normal and the observer's line of sight, serves as a useful indicator of a region's proximity to the disk center. Specifically,  $\mu$  ranges from 1 at the disk center to 0 at the limb (Thompson, 2006). Conducting CLV observations at previously unmeasured  $\mu$  values enables us to capture data from different regions across the disk, facilitating studies of how observational features vary with their position on the disk.

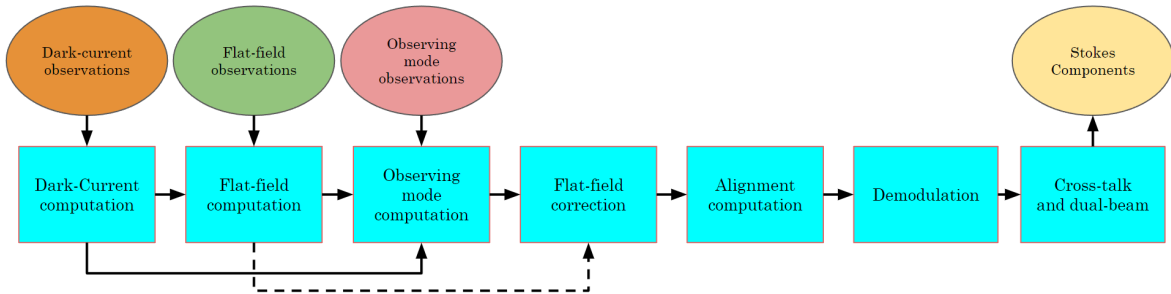


Figure 2.5 Block diagram of the standard reduction process: Blue boxes represent the individual steps that make up the reduction, while ellipses indicate the different sets of observations and the final product (yellow ellipse).

During the Sunrise III observation campaign, 38 timelines were run, including calibration timelines in addition to the scientific programs presented here. Some examples of the different targets employed during the campaign are shown in fig. 2.4. A detailed record of TuMag's observations can be found online both in the pipeline's repository and in TuMag's official data website<sup>†</sup>.

## 2.3 Pipeline

Before data can be employed for scientific purposes, it has to undergo a process where all the instrumental and spurious effects are removed and the necessary computations for the scientific aim are carried out. This process, usually referred to as data reduction, has to be specifically designed for each instrument, as the particular properties of the instrument come into play. Being a spectropolarimeter, TuMag's data reduction pipeline must, in addition to removing the instrumental artifacts, compute the stokes components of the incoming light.

In this section we introduce the software that has been developed for TuMag's data processing. Due to the proximity of the data's arrival to the end of this thesis, its important to note that the data reduction is still in development, with some calibration steps still undeveloped. In the following, we present the current status of the pipeline, along with a few examples of the results. The pipeline is publicly available in a GitHub repository<sup>‡</sup>.

### 2.3.1 Standard data reduction process.

The specific steps that have to be applied to a particular observation depends on the observation mode, and scientific aim of the observation, as different observations may require additional steps prior to the scientific exploitation. However, any observing mode that's

<sup>†</sup>[https://www.uv.es/jublanro/tumag\\_data\\_test.html](https://www.uv.es/jublanro/tumag_data_test.html)

<sup>‡</sup>[https://github.com/PabloSGN/TuMags\\_Reduction\\_Pipeline](https://github.com/PabloSGN/TuMags_Reduction_Pipeline)

employs either two of the modulation schemes, share a series of common steps that must be followed. Taking into account that save for the high cadence timelines, and the observing mode 0s, all observations follow this scheme, this is the process that the majority of TuMag data has to undergo.

These steps include the basic corrections that have to be applied to all images, namely flat-fielding and dark current corrections. But additionally, the final steps must combine the data from both cameras, and compute the stokes components. This process is illustrated in the block diagram in fig. 2.5 and consists of the following steps:

1. Dark current processing.
2. Flat-fielding processing.
3. Camera's alignment computation.
4. Processing of observing mode images (dark-current corrected).
5. Apply flat-field correction.
6. Demodulation.
7. Cross-talk correction and cameras combination.

The data reduction process begins with the dark-current processing, which involves averaging all individual dark frames within a specific set to generate a single dark-current frame per camera. This dark current is then subtracted from all images used in the reduction, including flat-fields, pinholes, and scientific observations, after rescaling the dark-current to the appropriate number of accumulations.

The second step is the flat-field computation. These observations, as previously mentioned, are a modified version of the nominal mode with an increased  $\lambda_{\text{rep}}$  and are repeated  $N_{\text{rep}}$  times. The processing involves averaging all images taken at a specific wavelength for the same modulation. Thus,  $\lambda_{\text{rep}} \times N_{\text{rep}}$  images are averaged to produce a single flat-field frame. To maintain spectral line information, flat-fields are normalized to their mean value, as flat-fields taken at the line core have lower intensity than those in the continuum. The goal is to correct intensity variations within a single frame without altering relative intensities across different spectral points.

Having computed the dark-current and the flat-fields, the scientific observations can be corrected by subtracting the dark-current and dividing the resulting image by the flat-field of the corresponding wavelength and modulation.

After flat-fielding and dark current correction, the different modulations and the two cameras are combined to infer the stokes components for every measured wavelength. However, in order to combine the data from different cameras and modulations, the images have to be aligned beforehand. The alignment is carried out with the already corrected images and consists on a sequential process where the four modulations of the camera one are first aligned, and then the images of the second camera are aligned with respect to the image of the camera one and the corresponding modulation. The alignment is performed at

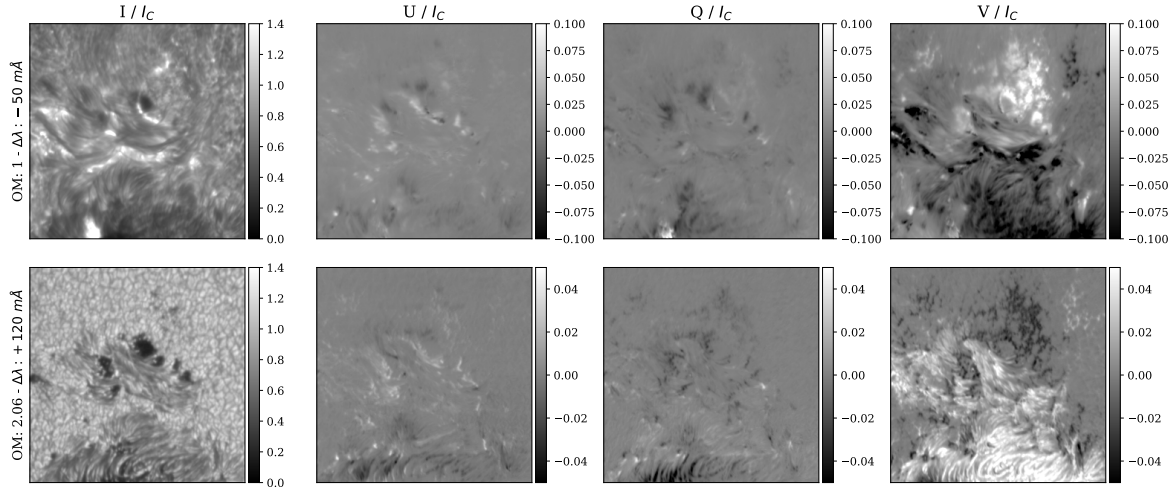


Figure 2.6 Stokes maps in magnesium and iron 525.06 nm lines wings, measured at  $-50 \text{ m}\text{\AA}$  and  $+120 \text{ m}\text{\AA}$  from the line core, respectively. The observation corresponds to a FS timeline ran in a flaring active region. Timestamp of the first observation mode (mode 1) : 2024/07/13 12:28:00.

subpixel accuracy employing the method described in Guizar-Sicairos et al. (2008), where the alignment is computed employing a two-dimensional cross-correlation in the Fourier domain.

After alignment, the Stokes components are derived through a process known as demodulation. This process is carried independently at different wavelengths and consists on a matrix multiplication employing the demodulation matrix and the four modulations. For the vectorial scheme this multiplication can be expressed as:

$$\begin{pmatrix} I \\ Q \\ U \\ V \end{pmatrix} = \underbrace{\begin{pmatrix} d_{00} & d_{01} & d_{02} & d_{03} \\ d_{10} & d_{11} & d_{12} & d_{13} \\ d_{20} & d_{21} & d_{22} & d_{23} \\ d_{30} & d_{31} & d_{32} & d_{33} \end{pmatrix}}_{\mathbf{D}} \begin{pmatrix} I_1 \\ I_2 \\ I_3 \\ I_4 \end{pmatrix}, \quad (2.1)$$

where the matrix  $\mathbf{D}$  is the inverse of the modulation matrix of the corresponding camera and pre-filter that were computed during the calibrations (see sec. ??). And for the longitudinal scheme:

$$\begin{pmatrix} I + V \\ I - V \end{pmatrix} = \begin{pmatrix} d_{00} & d_{01} \\ d_{10} & d_{11} \end{pmatrix} \begin{pmatrix} I_1 \\ I_2 \end{pmatrix}. \quad (2.2)$$

The result of the matrix multiplication is the Stokes components for each camera. However, the demodulation is never perfect due to small deviations of the demodulation matrix from the real one, or instrumental artifacts that have been uncorrected by the flat-fielding. These defects result in a contaminated Stokes components, where information from one component appears in other components, typically from Stokes  $I$  into  $Q$ ,  $U$ , and

or V. Nonetheless, these contamination, known as cross-talk, can be extracted from the data. Figure 2.6 shows an example of the demodulated stokes maps for an observing mode 1 (magnesium) and a 2.06 (iron 525.06 nm) at the wings of the spectral line, not corrected from cross-talk. The intensity map in the magnesium shows the beginning of a flare around the central sunspot.

The cross-talk correction is a manual process as different data sets require different corrections. For instance, some data sets may not show contamination from I to U while others do. Moreover, the correction might require to be applied using the information from the whole FoV or only of a small region. Thus, this is a correction that has to be carefully applied and it's hard to standardize to the whole set of observations. Nonetheless, the concept of the correction is the same.

The correction of the cross-talk from I to any other component starts by measuring the relation between the two components by fitting through a least-squares method, a polynomial of first order in order to compute the tendency, if there is one. Once this relation has been established, and the strength of the cross-talk (*i.e.* the value of the slope) measured, the correction is applied by simply, removing the tendency of the data:

$$S_{corr} = S_{orig} - (I_{orig} * a + b), \quad (2.3)$$

where the relation between the stokes component  $S_{orig}$  and stokes I  $I_{orig}$  has been fitted to the line:  $S_{orig} = I_{orig} * a + b$ . Figure 2.7 shows an example of a cross-talk correction in a small region of the FoV in the continuum of a quiet Sun observation. The granulation structure is clearly visible in Q and U before the correction, where no signal in linear polarization should be present. The central panel shows the dispersion between the corresponding stokes component and the intensity, along with the fitted relation. In the case of Q and U, the relation is stronger than in V, where the slope is almost 0. The right columns shows the result of the correction, with Q and U without the majority of influence of the intensity, although some traces can be found. Nevertheless, the cross-talk before the correction is below the 1%, and thus, the polarimetric sensitivity is larger than  $10^{-3}$ .

### 2.3.2 Extra calibration blocks.

As previously presented, TuMag observations include a series of calibrating observing modes that are not employed in the standard reduction process, namely, polarizers observations, both the lineal polarizer and the micropolarizers set, the pinholes observations, prefilter scans, or PD. These sets of calibrations are meant to be processed separately to aid with the data reduction in observing modes that require it.

The processing of these steps is still in an early stage, and are expected to be fully developed in the following months. However, we present now the idea of these observations and how they will be employed during the reduction process.

### 2.3.2.1 Image reconstruction.

The image reconstruction is in truth one of the steps in the main data's pipeline, and in the future it will be implemented as an additional step that has to be applied to all data sets to exploit the full potential of TuMag's spatial resolution. However, we have separated it in this description since it is not yet fully developed and ready to be automatically processed for all data sets.

The image reconstruction technique consists on deconvolving the PSF of the instrument from the data through a Wiener filter. PD measurements (see sec. 2.1.1.7) are employed to derive the PSF though the determination of the zernike parameters that describe the WFE. These PD measurements are taken before and after scientific observations to ensure the applicability of the reconstruction throughout the whole data series.

Figure 2.8 shows an example of such a reconstruction, for the 517 nm and 525.06 pre-filters. The reconstruction employs the closest PD measurement dataset to the observation and 21 zernikes for the PSF determination.

### 2.3.2.2 On-flight polarimetric calibration.

The presence of cross-talk in the observations can be originated from deviations of the modulation of the instrument with respect to the one derived during on-ground calibrations. In that case, the demodulation matrix employed in the pipeline deviates from the ideal one, resulting in a suboptimal demodulaion process. However, TuMag is equipped with both the linear polarizer and micropolarizer targets to assess the demodulation schemes.

Both polarizer targets can be employed to assess the level of cross-talk in continuum observations as no linear polarization should reach the detector in such cases. Thus, the level of signal in Q and U in such a scenario is a straightforward assessment of the closeness to the ideal demodulation scheme.

Moreover, the micropolarizer observations allow us to perform this assessment as a funciton of the region within the FoV. The micropolarizers are composed by arrays of 3x3 small linear polarizers oriented in different directions. Thus, the same assessment as the one employing the linear polarizer can be done but with each individual polarizer.

### 2.3.2.3 On-flight spectral calibration.

One of the most important calibration procedures that is still undeveloped is the on-flight spectral calibration or prefilter extraction. We know from the on ground calibrations and from the spectral scans taken during flight (see sect. 2.1.1.6) that the prefilters are not perfectly centered ant the measured instenisty is modified in different ways along the lines. In particular, magnesium line observations are the most affected by this. Figure 2.9 shows the average intensity along the spectral scan for the two most common observation modes in the observation campaign. The spectral profile of Obs. Mode 1 shows a continuum measurement with very low intensity due to both the prefilter and the etalon's second order contamination.

Although still undeveloped due to the lack of time, a correction addressing this issue

is planned for the near future. Employing the prefilter scans, where the spectral line is recorded with a rich spectral sampling and using an analytical model of the etalon's transmission profile, the contribution of both the second order and the effect of the prefilter can be carefully assessed through a fitting procedure. Software to carry out a very similar analysis has already been developed in other works. In the following chapters we delve into the theoretical modeling of etalons and the development of software to extract its contributions from the data. Minor modifications to this software will allow us to correct for both the aforementioned effects in TuMag's data.

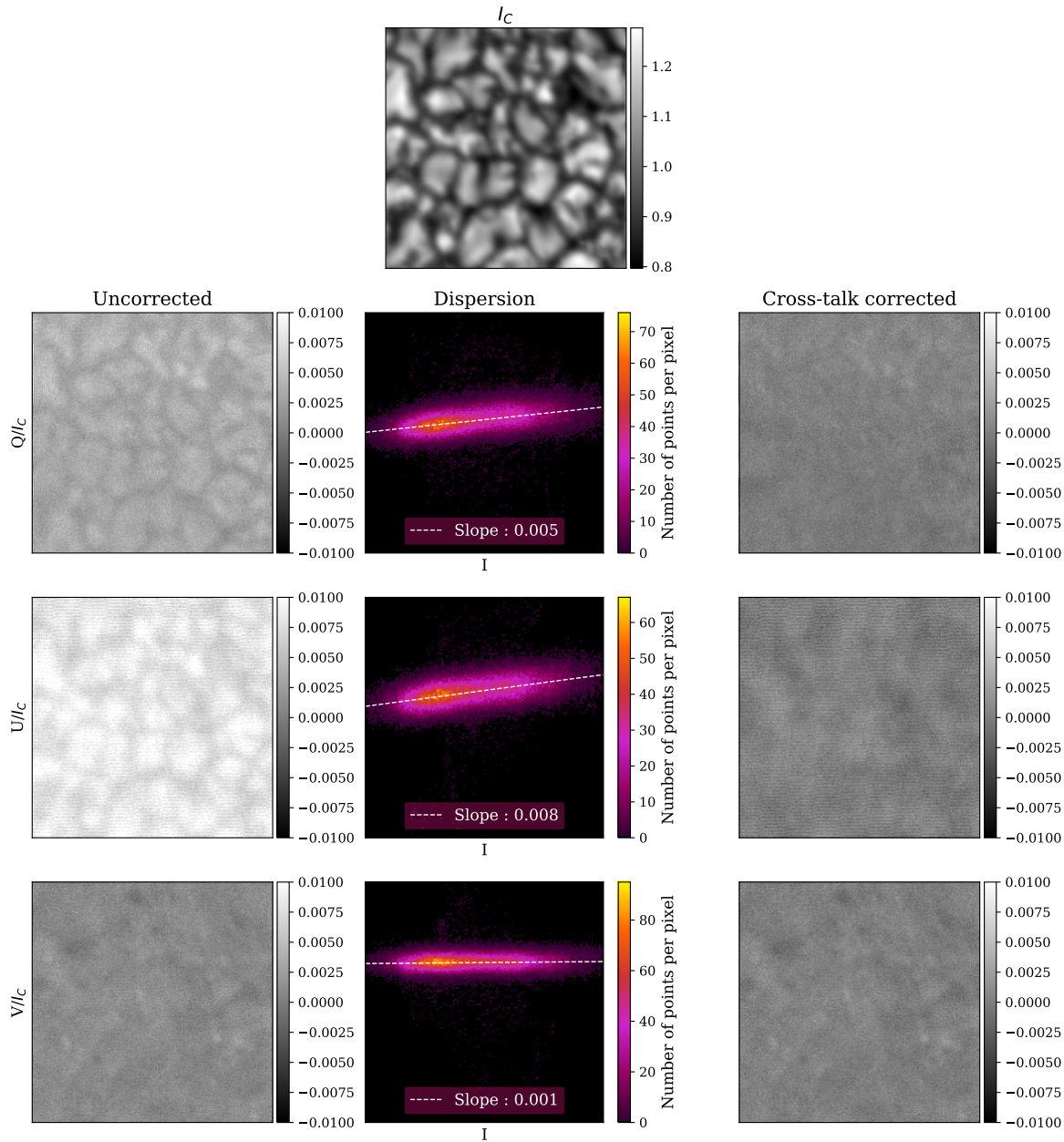


Figure 2.7 Example of a cross-talk correction in a small region of the FoV. Each row shows a different Stokes parameter. The left column shows quiet Sun Stokes maps after demodulation, the central column shows the dispersion between the intensity and the corresponding Stokes parameter, and the right column shows the corrected maps.

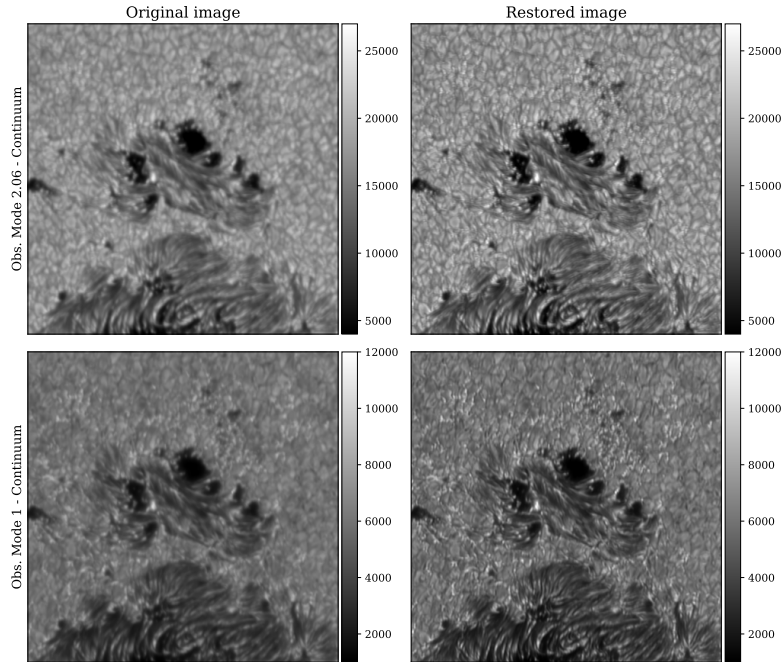


Figure 2.8 Example of image reconstruction in the FS timeline for both the 517 nm (Obs. Mode 1) and 525.06 nm (Obs. Mode 2.06) prefilters. The data set for the PD measurements was taken on the 13<sup>th</sup> at 11:42. The timestamp of the first image of the first observation mode is: 2024/07/13 12:28:00. PD computation made by F.J. Bailén.

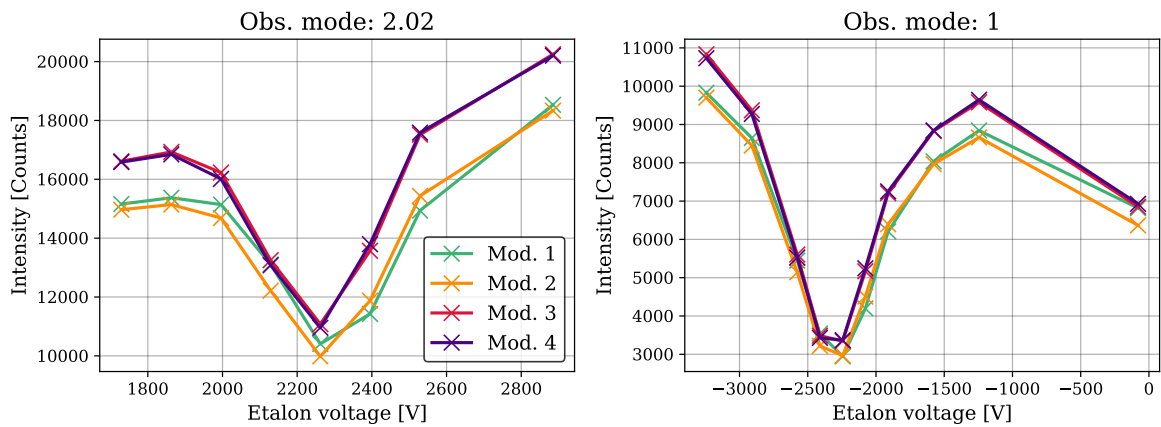
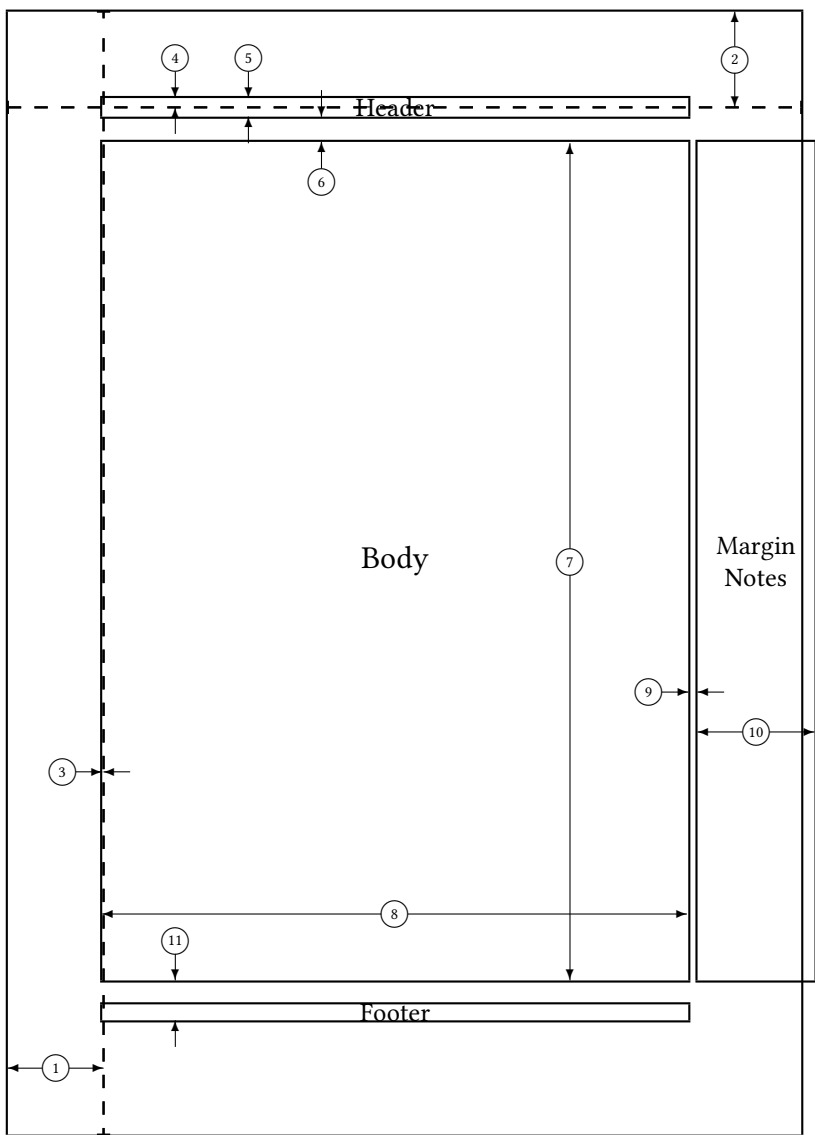


Figure 2.9 Average intensities along the iron 525.02 nm (mode 2.02) and magnesium (mode 1) lines. The different colors show the different modulations. The scans correspond to observations taken during the minimum success observations taken on the 2024/07/10 at 13:20.

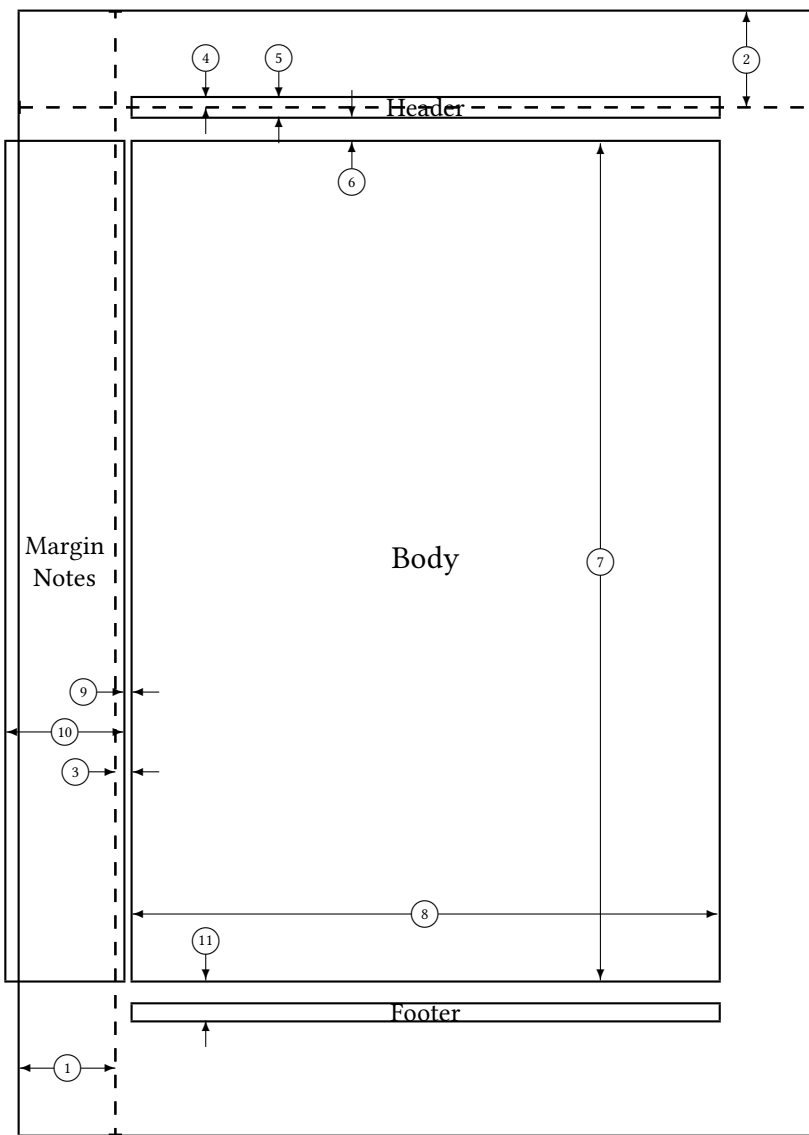
## BIBLIOGRAPHY

- Bailén, F. J., Orozco Suárez, D., Blanco Rodríguez, J., & del Toro Iniesta, J. C. Performance of Sequential Phase Diversity with Dynamical Solar Scenes. *Astrophys. J. Suppl.* **263**, 7 (2022).
- Bailén, F. J., Suárez, D. O., & del Toro Iniesta, J. On fabry-pérot etalon-based instruments. i. the isotropic case. *The Astrophysical Journal Supplement Series* **241**, 9 (2019).
- Barthol, P., Gandorfer, A., Solanki, S. K., et al. The sunrise mission. *Solar Physics* **268**, 1 (2011).
- Bianda, M., Solanki, S., & Stenflo, J. Hanle depolarisation in the solar chromosphere. *Astronomy and Astrophysics*, v. 331, p. 760-770 (1998) **331**, 760 (1998).
- Childlaw, R., Devaney, A., & Gonsalves, R. Analytical studies of phase estimation techniques, volume 1. *Final Technical Report* (1979).
- del Toro Iniesta, J. C. (2003), Introduction to spectropolarimetry (Cambridge university press).
- del Toro Iniesta, J. C., & Collados, M. Optimum modulation and demodulation matrices for solar polarimetry. *Applied Optics* **39**, 1637 (2000).
- del Toro Iniesta, J. C., & Ruiz Cobo, B. Inversion of the radiative transfer equation for polarized light. *Living Reviews in Solar Physics* **13**, 4 (2016).
- Gaskill, J. D. (1978), Linear systems, Fourier transforms, and optics, Vol. 56 (John Wiley & Sons).
- Guizar-Sicairos, M., Thurman, S. T., & Fienup, J. R. Efficient subpixel image registration algorithms. *Optics letters* **33**, 156 (2008).
- Helstrom, C. W. Image restoration by the method of least squares. *Josa* **57**, 297 (1967).
- Lakshminarayanan, V., & Fleck, A. Zernike polynomials: a guide. *Journal of Modern Optics* **58**, 545 (2011).
- Paxman, R. G., Schulz, T. J., & Fienup, J. R. Joint estimation of object and aberrations by using phase diversity. *JOSA A* **9**, 1072 (1992).

- Snyder, A. W. (1975), in Photoreceptor optics (Springer), 38–55.
- Solanki, S., Riethmüller, T., Barthol, P., et al. The second flight of the sunrise balloon-borne solar observatory: overview of instrument updates, the flight, the data, and first results. *The Astrophysical Journal Supplement Series* **229**, 2 (2017).
- Stokes, G. G. On the composition and resolution of streams of polarized light from different sources. *Transactions of the Cambridge Philosophical Society* **9**, 399 (1851).
- Thompson, W. Coordinate systems for solar image data. *Astronomy & Astrophysics* **449**, 791 (2006).
- Tyson, R. K. (2000), Introduction to adaptive optics, Vol. 41 (SPIE press).
- Uitenbroek, H. The accuracy of the center-of-gravity method for measuring velocity and magnetic field strength in the solar photosphere. *The Astrophysical Journal* **592**, 1225 (2003).
- Vargas Dominguez, S. Study of horizontal flows in solar active regions based on high-resolution image reconstruction techniques. *Ph. D. Thesis* (2009).
- Zernike, F. Diffraction theory of the knife-edge test and its improved form, the phase-contrast method. *Monthly Notices of the Royal Astronomical Society*, Vol. 94, p. 377-384 **94**, 377 (1934).



1 one inch + \hoffset	2 one inch + \voffset
3 \oddsidemargin = -1pt	4 \topmargin = -7pt
5 \headheight = 14pt	6 \headsep = 19pt
7 \textheight = 631pt	8 \textwidth = 441pt
9 \marginparsep = 7pt	10 \marginparwidth = 88pt
11 \footskip = 30pt	\marginparpush = 7pt (not shown)
\hoffset = 0pt	\voffset = 0pt
\paperwidth = 597pt	\paperheight = 845pt



1 one inch + \hoffset	2 one inch + \voffset
3 \evensidemargin = 13pt	4 \topmargin = -7pt
5 \headheight = 14pt	6 \headsep = 19pt
7 \textheight = 631pt	8 \textwidth = 441pt
9 \marginparsep = 7pt	10 \marginparwidth = 88pt
11 \footskip = 30pt	\marginparpush = 7pt (not shown)
\hoffset = 0pt	\voffset = 0pt
\paperwidth = 597pt	\paperheight = 845pt